

Attractive Hofstadter-Hubbard model with imbalanced chemical and vector potentials

M. Iskin

Department of Physics, Koç University, Rumelifeneri Yolu, 34450 Sarıyer, Istanbul, Turkey.

(Dated: March 30, 2015)

We study the interplay between the Hofstadter butterfly, strong interactions and Zeeman field within the mean-field Bogoliubov-de Gennes theory in real space, and explore the ground states of the attractive single-band Hofstadter-Hubbard Hamiltonian on a square lattice, including the exotic possibility of imbalanced vector potentials. We find that the cooperation between the vector potential and superfluid order breaks the spatial symmetry of the system, and flourish stripe-ordered Fulde-Ferrell-Larkin-Ovchinnikov (FFLO)-like superfluid and supersolid phases that can be distinguished and characterized according to their coexisting pair-density (PDW), charge-density (CDW) and spin-density (SDW) wave orders. We also discuss confined systems and comment on the likelihood of observing such stripe-ordered phases by loading neutral atomic Fermi gases on laser-induced optical lattices under laser-generated artificial gauge fields.

PACS numbers: 03.75.Ss, 03.75.Hh, 67.85.-Lm, 67.85.-d, 67.80.kb

I. INTRODUCTION

The exact energy spectrum of a single quantum particle that is confined to move on a two-dimensional tight-binding periodic lattice under the influence of a uniform magnetic flux has been known for a long time [1, 2], where the competition between the lattice spacing and cyclotron radius gives rise to a self-similar complex pattern of sub-bands and mini-gaps. However, regardless of all efforts since the prediction of this Hofstadter spectrum, there has been very recent but still limited success in observing some of its signatures in graphene-based solid-state materials with artificially-engineered superlattices under real magnetic fields [3, 4]. In addition, thanks to the recent realisation of artificial gauge fields in atomic systems [5–12], there is also an increasing interest on this subject from the cold-atom community [13–20]. In particular, by engineering spatially-dependent complex tunneling amplitudes with laser-assisted tunneling and a potential energy gradient, two groups have recently reported realisation of the Hofstadter-Harper Hamiltonian using neutral rubidium atoms that are loaded into laser-induced periodic potentials [16–18].

Even though the Hofstadter and Hubbard Hamiltonians have themselves been the subject of many works in the literature, there has been a lack of interest in the combined Hofstadter-Hubbard Hamiltonian even at the mean-field level. For instance, while the use of momentum-space BCS formalism limits previous analysis of the attractive Hofstadter-Hubbard model only to vortex lattice (VL) configurations [21], the existence of pair-density wave (PDW) and VL orders have been proposed in the context of a somewhat related model: an anisotropic 3D continuum Fermi gas experiencing a uniform magnetic flux [22]. By first limiting their description to the lowest-Landau-level limit and then making further assumptions about the strength of the anisotropic trap, the authors obtain an effectively a 1D Hamiltonian in momentum space, and solved it using the BCS formalism. The existence and characterisation of a variety of distinct stripe-ordered many-body phases have either been overlooked or gone unnoticed until very recently [23], distinguishing our work from the literature.

In particular, here we use Bogoliubov-de Gennes (BdG)

theory in real space and study the mean-field ground states of the attractive single-band Hofstadter-Hubbard Hamiltonian on a square lattice, including the effects of imbalanced chemical and vector potentials. We find that the cooperation between the vector potentials and interaction breaks the spatial symmetry of the system, leading to various stripe-ordered superfluid (SF) and supersolid (SS) phases that can be distinguished and characterized according to their coexisting PDW, charge-density (CDW) and spin-density (SDW) wave orders. We also discuss possible observation of such stripe-ordered phases by confining neutral atomic Fermi gases in laser-induced optical lattices under laser-generated artificial gauge fields.

The rest of this paper is organised as follows. In Sec. II, first we introduce the physical setting of the problem and the model Hamiltonian used, then review the non-interacting Hofstadter Hamiltonian and its well-known Hofstadter spectrum, and then describe the self-consistent BdG formalism which takes fermion-fermion interactions into account within the mean-field approximation for pairing. The resultant BdG equations are solved in Sec. III, where first we tabulate the numerically obtained mean-field ground states, paying a special attention to the striped phases in the dimer-BEC limit, and then construct the thermodynamic phase diagrams. The effects of Hartree shifts on the possible ground states are discussed in Sec. V in the context of harmonically-confined atomic systems. We end the paper with a briery summary of our conclusions and an outlook in Sec. VI, and an Appendix comparing the dimer-BEC limit in the Landau and symmetric gauges.

II. THEORETICAL FRAMEWORK

To explore the ground states of the single-band Hofstadter-Hubbard model, we start with

$$H = - \sum_{ij\sigma} t_{ij\sigma} a_{i\sigma}^\dagger a_{j\sigma} - \sum_{i\sigma} \mu_{i\sigma} a_{i\sigma}^\dagger a_{i\sigma} - g \sum_i a_{i\uparrow}^\dagger a_{i\uparrow} a_{i\downarrow}^\dagger a_{i\downarrow}, \quad (1)$$

and consider both thermodynamic and confined systems. Here, $a_{i\sigma}^\dagger$ ($a_{i\sigma}$) creates (annihilates) a $\sigma \equiv \{\uparrow, \downarrow\}$ fermion on site i , $t_{ij\sigma}$ is its hopping parameter from site i to j , and $\mu_{i\uparrow} = \mu - V_i + h$ and $\mu_{i\downarrow} = \mu - V_i - h$ are effectively their local chemical potentials in the presence of confining potential V_i and an out-of-plane Zeeman field h . We assume $h \geq 0$ without loosing generality, since $h < 0$ results can be easily deduced by letting $\uparrow \rightarrow \downarrow$ and $\downarrow \rightarrow \uparrow$. The density-density interaction term is taken to be local (on-site) and attractive with strength $g \geq 0$, and the resultant many-body phases are investigated within the mean-field approximation for the Cooper pairs and their superfluidity, as described below.

A. Mean-Field Hofstadter-Hubbard Hamiltonian

In particular, we analyse the following mean-field Hamiltonian for square lattices,

$$H_{mf} = - \sum_{ij\sigma} t_{ij\sigma} a_{i\sigma}^\dagger a_{j\sigma} - \sum_{i\sigma} \tilde{\mu}_{i\sigma} a_{i\sigma}^\dagger a_{i\sigma} + \sum_i \left(\Delta_i a_{i\uparrow}^\dagger a_{i\downarrow}^\dagger + \Delta_i^* a_{i\downarrow} a_{i\uparrow} + \frac{|\Delta_i|^2}{g} \right), \quad (2)$$

where $\tilde{\mu}_{i\uparrow} = \mu_{i\uparrow} - gn_{i\downarrow}$ and $\tilde{\mu}_{i\downarrow} = \mu_{i\downarrow} - gn_{i\uparrow}$ take the Hartree shifts into account. Here, $n_{i\sigma} = \langle a_{i\sigma}^\dagger a_{i\sigma} \rangle$ is the average number of σ fermions where $\langle \dots \rangle$ is a thermal average, and the remaining terms in Eq. (2) involve the complex SF order parameter $\Delta_i = g \langle a_{i\uparrow}^\dagger a_{i\downarrow}^\dagger \rangle$. These average quantities are specified below in Eqs. (7)-(9), and we use them in Sec. III for characterising the state of the system.

The complex hopping parameters are assumed to connect only the nearest-neighbor sites, i.e, $t_{ij\sigma} = t_\sigma e^{i\theta_{ij\sigma}}$ where the amplitudes $t_\uparrow = t_\downarrow = t \geq 0$ are taken to be equal for i and j nearest neighbors and 0 otherwise. The phase, however, depends on the external magnetic (or artificial gauge) field experienced by σ fermions. In particular, we use the Peierls substitution and take $\theta_{ij\sigma} = (1/\phi_0) \int_{\mathbf{r}_i}^{\mathbf{r}_j} \mathbf{A}_\sigma(\mathbf{r}) \cdot d\mathbf{r}$, with $\phi_0 = 2\pi\hbar/e$ the magnetic flux quantum and $\mathbf{A}_\sigma(\mathbf{r})$ the vector potential which is assumed to be independently controllable for \uparrow and \downarrow fermions. Note that while independent control of $\mathbf{A}_\sigma(\mathbf{r})$ is not possible for conventional solid-state materials with real magnetic fields where σ corresponds to the \pm projections of spin angular momentum of electrons, such a control can be achieved with neutral atomic systems under the influence of laser-generated artificial gauge fields where pseudo-spin σ is just a label for two of the hyperfine states of a particular atom. In this paper, we choose Landau gauge for the vector potential, i.e, $\mathbf{A}_\sigma(\mathbf{r}) \equiv (0, B_\sigma x, 0)$, leading to a uniform magnetic flux $\Phi_\sigma = B_\sigma \ell^2$ per unit cell penetrating our square lattice, where ℓ is the lattice spacing. Denoting (x, y) coordinates of site i by $(n\ell, m\ell)$, this gauge simply implies $\theta_{ij\sigma} = 0$ and $\theta_{ij\sigma} = \pm 2\pi n\phi_\sigma$ for links along the x and y directions, respectively, where $\phi_\sigma = \Phi_\sigma/(2\pi\phi_0)$ characterizes the competition between ℓ and the magnetic length scale (cyclotron radius) $\ell_{B_\sigma} = \sqrt{\hbar/(eB_\sigma)}$. We note that while $\phi_\uparrow = \phi_\downarrow \ll 1$ for typical electronic crystals, even for the

largest magnetic field $B_\uparrow = B_\downarrow \sim 100T$ that is attainable in a laboratory, ϕ_\uparrow and ϕ_\downarrow may be tuned at will in atomic optical lattices.

Let us first set $g = 0$ and $\mu_{i\sigma} = 0$ in Eq. (2), and review the well-known single-particle problem, i.e, the Hofstadter Hamiltonian for a uniform square lattice.

B. Hofstadter Butterfly (HB)

In the non-interacting limit, the single-particle Hofstadter-Hamiltonian describing a σ fermion can be written as,

$$H_{0\sigma} = -t_\sigma \sum_{nm} \left(a_{nm\sigma}^\dagger a_{n+1,m\sigma} + e^{i2\pi\phi_\sigma n} a_{nm\sigma}^\dagger a_{n,m+1,\sigma} + \text{H.c.} \right), \quad (3)$$

where H.c. is the Hermitian conjugate. For rational values of $\phi_\sigma \equiv p_\sigma/q_\sigma$, where p_σ and q_σ are positive integers with no-common factor, i.e, co-prime numbers, while $H_{0\sigma}$ maintains its translational invariance in the y direction, it requires q_σ sites for translational invariance in the x direction. Thanks to the Bloch theorem, the 1st magnetic Brillouin zone is determined by $-\pi \leq k_y \ell \leq \pi$ and $-\pi/q_\sigma \leq k_x \ell \leq \pi/q_\sigma$, and this increased periodicity motivates us to work with a supercell of $1 \times q_\sigma$ sites. The excitation spectrum is determined by solving the Schrödinger equation $H_{0\sigma} \Psi_\sigma = \varepsilon(\phi_\sigma) \Psi_\sigma$ for all momentum $\mathbf{k} \equiv (k_x, k_y)$ values in the 1st magnetic Brillouin zone. Denoting the components of the wave function as $\Psi_\sigma = (\psi_1^*, \psi_2^*, \psi_3^*, \dots, \psi_{q_\sigma}^*)^\dagger$, where ψ_n corresponds to the n th site of the supercell, the $q_\sigma \times q_\sigma$ Hamiltonian matrix at a given \mathbf{k} value

$$\begin{bmatrix} C_{1\sigma} & T_\sigma^* & 0 & \cdot & \cdot & 0 & T_\sigma \\ T_\sigma & C_{2\sigma} & T_\sigma^* & 0 & \cdot & \cdot & 0 \\ 0 & T_\sigma & C_{3\sigma} & \cdot & \cdot & \cdot & \cdot \\ \cdot & \cdot & \cdot & \cdot & \cdot & \cdot & 0 \\ 0 & \cdot & \cdot & \cdot & \cdot & C_{n-1,\sigma} & T_\sigma^* \\ T_\sigma^* & 0 & \cdot & \cdot & 0 & T_\sigma & C_{n\sigma} \end{bmatrix} \quad (4)$$

describes the supercell with periodic Bloch boundary conditions. Here, $C_{n\sigma} = -2t_\sigma \cos(k_y \ell + 2\pi n p_\sigma/q_\sigma)$ and $T_\sigma = -t_\sigma e^{ik_x \ell}$.

The eigenvalues $\varepsilon(\phi_\sigma)$ of this $q_\sigma \times q_\sigma$ matrix can be numerically obtained for any given rational number ϕ_σ and the energy spectrum $\varepsilon(\phi_\sigma)$ vs. ϕ is known as HB [1, 2]. The spectrum is shown in Fig. 1, where, for a given ϕ_σ , it consists of non-overlapping q_σ bands with $q_\sigma + 1$ energy gaps in between, and each one of these q_σ bands can accommodate $1/q_\sigma$ particle filling with a total filling of 1. Therefore, if we index energy gaps as $z_\sigma = \{0, 1, 2, \dots, q_\sigma\}$, starting from the bottom edge of the band in such a way that the lowest ($z_\sigma = 0$) and highest ($z_\sigma = q_\sigma$) gaps correspond, respectively, to a particle vacuum and a fully-filled band insulator, particle fillings within all of these gapped regions can be compactly written as z_σ/q_σ . Note that while all gaps are open for odd q_σ , the middle $z_\sigma = q_\sigma/2$ gap corresponding to a half-filled lattice

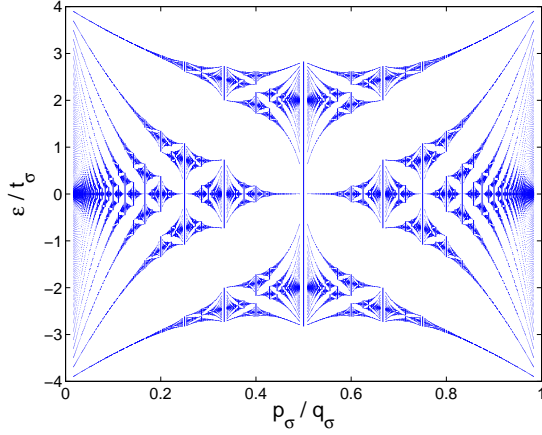


FIG. 1. (Color online) The Hofstadter spectrum ε/t_σ is presented as a function of $\phi_\sigma = p_\sigma/q_\sigma$, showing its fractal structure with numerous sub-bands and mini-gaps.

is not open when q_σ is even, and therefore, a half-filled lattice is not an insulator for any q_σ . In the $\phi_\sigma \rightarrow 0$ limit, the HB spectrum recovers the usual tight-binding dispersion of cosines $\varepsilon_{\mathbf{k}\sigma} = -2t_\sigma [\cos(k_x\ell) + \cos(k_y\ell)]$, which has an energy bandwidth $W_\sigma = 8t_\sigma$.

Since ℓ and ℓ_{B_σ} are the only two length scales in Eq. (3) such that $\phi_\sigma = \ell^2/(2\pi\ell_{B_\sigma}^2)$, the fractal structure of HB is clearly a result of their competition. In addition, each \mathbf{k} state is q_σ -fold degenerate in the 1st magnetic Brillouin zone (not explicitly shown in the figure), i.e.,

$$\varepsilon_{b,k_x,k_y}(\phi_\sigma) = \varepsilon_{b,k_x,k_y+2\pi\phi_\sigma f/\ell}(\phi_\sigma) \quad (5)$$

with $b = 1, 2, \dots, q_\sigma$ labelling the bands and $f = 1, 2, \dots, q_\sigma$ labelling the degenerate \mathbf{k} states. We have recently shown that the HB spectrum plays a crucial role in determining the many-body states of the interacting system [23], and our primary objective here is to extend and generalise the analysis to imbalanced gauge fields.

C. Bogoliubov-de Gennes (BdG) Theory

For this purpose, we diagonalise Eq. (2) via the Bogoliubov-Valatin transformation, i.e., $a_{i\sigma} = \sum_m (u_{mi\sigma}\gamma_{m\sigma} - s_\sigma v_{mi\sigma}^*\gamma_{m,-\sigma}^\dagger)$, where $\gamma_{m\sigma}^\dagger$ ($\gamma_{m\sigma}$) creates (annihilates) a pseudo-spin σ quasiparticle with energy ϵ_m^σ and wave functions $u_{mi\sigma}$ and $v_{mi\sigma}$, and $s_\uparrow = +1$ and $s_\downarrow = -1$. The resultant BdG equations can be compactly written as,

$$\sum_j \begin{pmatrix} -t_{ij\uparrow} - \tilde{\mu}_{i\uparrow}\delta_{ij} & \Delta_i\delta_{ij} \\ \Delta_i^*\delta_{ij} & t_{ij\downarrow}^* + \tilde{\mu}_{i\downarrow}\delta_{ij} \end{pmatrix} \varphi_{mj}^\sigma = s_\sigma \epsilon_m^\sigma \varphi_{mi}^\sigma, \quad (6)$$

where δ_{ij} is the Kronecker delta, and $\varphi_{mi}^\uparrow = (u_{mi\uparrow}^*, v_{mi\downarrow}^*)^\dagger$ and $\varphi_{mi}^\downarrow = (v_{mi\uparrow}, -u_{mi\downarrow})^\dagger$ are the corresponding eigenfunctions for $\epsilon_m^\sigma \geq 0$ eigenvalue. Note that the BdG equations are invariant under the transformation $v_{mi\uparrow} \rightarrow u_{mi\uparrow}^*$,

$u_{mi\downarrow} \rightarrow -v_{mi\downarrow}^*$ and $\epsilon_{m\downarrow} \rightarrow -\epsilon_{m\uparrow}$, and therefore, it is sufficient to solve only for $u_{mi} \equiv u_{mi\uparrow}$, $v_{mi} \equiv v_{mi\downarrow}$ and $\epsilon_m \equiv \epsilon_m^\uparrow$ as long as all solutions with positive and negative ϵ_m are kept.

Using the transformation, the complex order parameter Δ_i can be written as

$$\Delta_i = -g \sum_m u_{mi} v_{mi}^* f(\epsilon_m), \quad (7)$$

where $f(x) = 1/[e^{x/(k_B T)} + 1]$ is the Fermi function with k_B the Boltzmann constant and T the temperature. Equations (6) and (7) have to be solved self-consistently for a given μ and h , such that the total number of σ fermions satisfies $N_\sigma = \sum_i n_{i\sigma}$. Here, $0 \leq n_{i\sigma} = \langle a_{i\sigma}^\dagger a_{i\sigma} \rangle \leq 1$ is the average number of σ fermions on site i , and using the transformation, it can be written as

$$n_{i\uparrow} = \sum_m |u_{mi}|^2 f(\epsilon_m), \quad (8)$$

$$n_{i\downarrow} = \sum_m |v_{mi}|^2 f(-\epsilon_m), \quad (9)$$

for the \uparrow and \downarrow fermions, respectively. We note that unlike the continuum models where the solutions of the self-consistency equations depend explicitly on the high-momentum cut-off, requiring a high-energy regularisation in order to obtain cut-off independent results, the lattice versions given in Eqs. (7)-(9) do not require such a regularisation, since the lattice spacing ℓ already provides an implicit short-distance cut-off.

In the absence of gauge fields when $\theta_{ij} = 0$, it is generally accepted that the mean-field description given above provides qualitative understanding either at low temperatures ($T \ll T_c$) for any g or for weak $g \lesssim W$ at any T , where T_c is the critical SF transition temperature. It is also known that single-band Hubbard models gradually become inadequate in describing strongly-interacting cold-atom systems on optical lattices, requiring multi-band models [24]. In addition, the real-space BdG theory goes beyond the standard local-density approximation since it includes both θ_{ij} and V_i exactly into the mean-field theory without relying on further approximations. Hoping to shed light on the qualitative effects of gauge fields on the ground states of Eq. (2), here we mainly concentrate on weak and intermediate g at $T = 0$ as discussed next.

III. NUMERICAL FRAMEWORK

In order to explore the possible phases, let us set $V_i = 0$ and consider a uniform $45\ell \times 45\ell$ square lattice, which is large enough to construct the thermodynamic phase diagrams for $\phi_\sigma = \{0, 1/6, \pm 1/4\}$. We note that even though our phase diagrams are reliable, the phase boundaries should be taken as qualitative guides to the eye due to the possibility of minor finite-size effects. We neglect the Hartree shifts for the moment because not only the self-consistent solutions converge much faster but also the resultant phase diagrams are much more easier to interpret and understand. In addition, since none of the PDW, CDW and SDW instabilities are driven by these shifts, our qualitative mean-field results already paves

TABLE I. While the S-SS* phase has a small but finite sign-changing striped-SDW order, the system is globally unpolarized very much like the unpolarized uniform superfluid (U-SF) or unpolarized striped supersolid (S-SS) phase.

| Phase | $ \Delta_i $ | $n_{i\uparrow} + n_{i\downarrow}$ | $n_{i\uparrow} - n_{i\downarrow}$ | ϕ_σ |
|-------|--------------|-----------------------------------|-----------------------------------|--|
| U-SF | Uniform | Uniform | 0 | $\phi_\uparrow = -\phi_\downarrow$ |
| S-SF | PDW | 1 | 0 | $\phi_\uparrow = \phi_\downarrow$ |
| S-SS | PDW | CDW | 0 | $\phi_\uparrow = \phi_\downarrow$ |
| S-SS* | PDW | CDW | SDW | $ \phi_\uparrow \neq \phi_\downarrow $ |
| P-SF | | otherwise | | |

the way to quantitative understanding of the possible ground states of Eq. (2). However, see Sec. VB for the effects of Hartree shifts on confined systems.

For this purpose, we numerically solve Eqs. (6)-(9) at $T = 0$, and obtain self-consistent solutions of Δ_i/t and $n_{i\sigma}$ as functions of g/t , μ/t , h/t and ϕ_σ . This can be achieved numerically via the iterative method of relaxation as follows. For a given set of parameters, first (i) start with an input set of Δ_i , then (ii) construct the BdG matrix given in Eq. (6), and then (iii) use its eigenstates in Eq. (7) to generate a new set of Δ_i , and finally (iv) repeat these steps until the input and output sets of Δ_i lie within a confidence level. Once this iterative method converges, (v) use Eqs. (8)-(9) to calculate $n_{i\sigma}$. It turns out that while Eqs. (6)-(9) have unique solutions in the low- h/g limit, they in general allow for multiple solutions for the polarized many-body phases, and therefore, it is essential to try several initial sets of Δ_i and verify the (meta)stability of the solutions.

A. Ground-State Phases

Depending on the spatial profiles of $|\Delta_i|$, $n_{i\uparrow}$ and $n_{i\downarrow}$, we distinguish the single-particle band insulator and normal phases from the ordered many-body ones using the following criteria. When h/g is sufficiently high that $\Delta_i \rightarrow 0$ (precisely speaking $|\Delta_i| < 10^{-3}t$ in our numerics) for every i , the ground state can be a σ -vac phase which is a vacuum of σ component with $n_{i\sigma} = 0$, a σ - $I(m/n)$ phase which is a band insulator of σ component with uniform $n_{i\sigma} = m/n$, a σ - N phase which is a normal σ component, or an $\uparrow\downarrow$ - PN phase which is a polarized normal mixture of \uparrow and \downarrow components. We checked in our numerics that while σ - N and $\uparrow\downarrow$ - PN phases have slightly non-uniform $n_{i\sigma}$ for $\phi \neq 0$, the C_4 symmetry of the square lattice is preserved. On the other hand, when h/g is sufficiently low that $\Delta_i \neq 0$ (i.e., $|\Delta_i| > 10^{-3}t$) for some i , the ground states can be characterized according to Table I. Unlike our earlier work [23], here we do not finely classify the polarized superfluid (P-SF) phase depending on the coexisting (striped or non-striped) PDW, CDW, SDW and/or VL orders. Instead, we focus mostly on the existence of striped phases in the dimer-BEC limit as the main message of this manuscript, for which physical (analytical) insight are also given.

The globally-unpolarized states are denoted by U-SF, S-

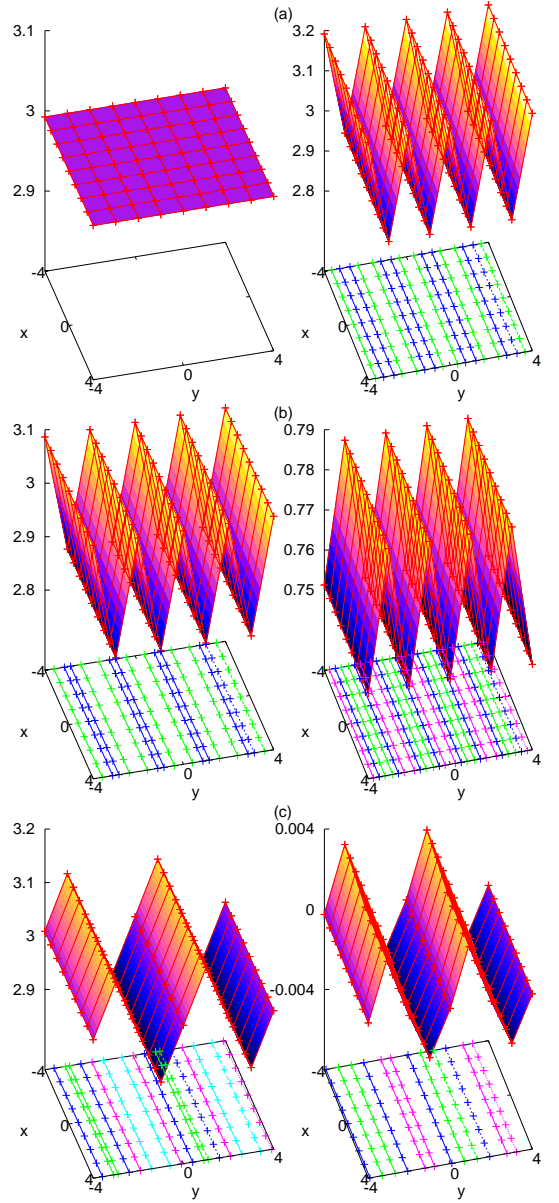


FIG. 2. (Color online) Characterisation of globally-unpolarized many-body phases. (a) Typical $|\Delta_i|/t$ profiles are shown for the U-SF (left) and S-SF phases (right), where $\phi_\uparrow = -\phi_\downarrow = 1/4$ and $\phi_\uparrow = \phi_\downarrow = 1/4$, respectively, and $\mu = 0$ (uniformly half-filled) in both figures. (b) Typical $|\Delta_i|/t$ (left) and $n_{i\uparrow} + n_{i\downarrow}$ (right) profiles are shown for the S-SS phase, where $\phi_\uparrow = \phi_\downarrow = 1/4$ and $\mu = -t$. (c) Typical $|\Delta_i|/t$ and $n_{i\uparrow} - n_{i\downarrow}$ profiles are shown for the S-SS* phase, where $\phi_\uparrow = 0$, $\phi_\downarrow = 1/4$ and $\mu = -t$. Note in (c) that even though the system is globally unpolarized, it has both SDW and CDW (not shown) orders. Here, (x, y) are in units of ℓ , and we set $h = 0$ and $g = 7t$ in all figures.

SF and S-SS, and they stand, respectively, for uniform-SF, striped-SF, and striped-SS. The S-SS* state is also globally unpolarized, very much like the S-SS phase but it has an additional sign-changing striped-SDW order driven by the imbalance between ϕ_\uparrow and ϕ_\downarrow . For instance, typical $|\Delta_i|$ and $n_{i\uparrow} \pm n_{i\downarrow}$ profiles are illustrated in Fig. 2 for all of them. De-

pending on μ , h , ϕ_\uparrow and ϕ_\downarrow , one of the U-SF, S-SF, S-SS and S-SS* phases always appears in the thermodynamic phase diagrams beyond a critical g/t threshold, as discussed next.

B. Dimer-BEC Limit in the Landau Gauge

When $g/t \gg 1$ is sufficiently high, the physics must eventually be determined by the two-body bound states, i.e., Cooper pairs become bosonic dimers, and unless $g/t \rightarrow \infty$, the dimer-dimer interaction [$g_{dd} \sim (t_\uparrow^2 + t_\downarrow^2)/g$] is finite. Such weakly-repulsive dimers can effectively be described by the Hofstadter-Bose-Hubbard model, where superfluidity has recently been shown to break translation symmetry in the weakly-interacting limit [25].

In the ideal-dimer limit of our model Hamiltonian, the only way a tightly-bound dimer to move from a site i to j in the lattice is via what is known as pair-breaking mechanism, i.e., virtual ionisation of its constituents costs a penalty of g , and this gives rise to the effective dimer hopping parameter $t_{ijd} = 2t_{ij\uparrow}t_{ij\downarrow}/g$. Therefore, the effective hopping amplitude and gauge field of the dimers can be written as $t_d \approx 2t_\uparrow t_\downarrow/g$ and $\phi_d = \phi_\uparrow + \phi_\downarrow = p_d/q_d$, respectively, where $p_d = (p_\uparrow q_\downarrow + p_\downarrow q_\uparrow)/Q$ and $q_d = q_\uparrow q_\downarrow/Q$. Here, Q is a positive integer number chosen such that p_d and q_d are coprime numbers, and it depends on the entire $\{p_\uparrow, p_\downarrow, q_\uparrow, q_\downarrow\}$ set. Since HB for dimers is q_d -fold degenerate, their BEC order parameter has contributions from all degenerate $\mathbf{k}_d = \{(0, 0); (0, 2\pi\phi_d f/\ell)\}$ momenta, where $f = 1, \dots, q_d - 1$ such that $\Psi_{id} = c_0 + \sum_f c_f e^{i2\pi\phi_d f i_y/\ell}$ and $c_f = |c_f|e^{i\vartheta_f}$ are complex variational parameters. However, unlike atomic bosons where all of the degenerate states have equal weight, dimer bosons are fermion pairs and the number of ways of creating them with $k_{yd} = k_{y\uparrow} + k_{y\downarrow}$ momentum depends on f , ϕ_\uparrow and ϕ_\downarrow . For instance, there are $2(q - f) - 1$ ways of intra-band pairing when $\phi_\uparrow = \phi_\downarrow = p/q$ and q is even. Thus, this analysis show that higher k_{yd} states contribute less and less, forming a perturbative series.

It turns out that the first order ($f = 1$) correction is already much smaller than the zeroth order ($f = 0$) one, and that the $f \geq 2$ terms are always negligible when g/t is sufficiently large. This is because all of our numerical results fit quite well with

$$|\Delta_i| = |\Delta_0| + |\Delta_1| [1 - \cos(2\pi\phi_d i_y/\ell)], \quad (10)$$

in the entire globally-unpolarized region, including S-SF, S-SS and S-SS* phases. Here, the $\mathbf{k}_d = (0, 0)$ contribution $|\Delta_0| = (g/2 - 4t^2/g)\sqrt{n(2-n)}$ is uniform in space and determined by the total average filling n with $\mu = (g/2 - 8t^2/g)(n - 1)$ [26], $|\Delta_1| \approx t^2/g$ for $\mu \approx 0$, and i_y is the y coordinate of site i . Moving towards the BCS side, the second-order correction to Eq. (10) can be shown to be $+|\Delta_2| \cos(4\pi\phi_d i_y/\ell)$ for even q_d . Since this term is in- (out-of- π -) phase with the zeroth (first) order term, it tends to open throughs along the peaks arised from the first order one, suggesting that $\vartheta_f - \vartheta_0 = \pi f$, i.e., the form of $|\Psi_{id}|$ coincides with $|\Delta_i|$ under these conditions. Equation (10) clearly shows that modulations of $|\Delta_i|$ have a spatial period of q_d lattice sites

along the y direction. It also implies that it is the cooperation between ϕ_d and g that is responsible for the broken spatial symmetry and appearance of stripe order, and even though the stripe order gradually fades away with increasing g , it survives even in the $g \gg W$ limit as long as g/t is finite.

Thus, this analysis suggests that the existence of stripe-ordered SF and SS phases is not an artefact of the mean-field description, and they are physically expected in the dimer-BEC limit of the attractive Hofstadter-Hubbard model, as discussed next.

IV. THERMODYNAMIC PHASE DIAGRAMS

Despite tremendous efforts over several decades, while the exact phase diagram of even the simplest Hubbard model (which does not include the gauge fields or Zeeman fields) is still the subject of a hot debate, the mean-field phases and resultant phase diagrams of the mean-field Hubbard model are pretty much settled. To appreciate the effects of gauge fields, first we study Eq. (2) with $\phi_\uparrow = \phi_\downarrow = 0$.

A. No Gauge Fields: $\phi_\uparrow = \phi_\downarrow = 0$

Our results for this limit is presented in Fig. 3, where we set $\mu = 0$ in 3(a) corresponding to a half-filled lattice, and $\mu = -t$ in 3(b). We find that the phase diagrams are very similar, and depending on the particular value of g , there are two critical h fields. Since FFLO phase occupies a tiny parameter space near the normal phase boundary and only on the BCS side when $g/t \lesssim W$, we do not finely classify the character of P-SF phase in Fig. 3 and throughout this paper. The U-SF phase, where $\Delta_i = \Delta_0$ for all i , turns into a P-SF beyond a first critical field h_{c1} , and then the P-SF phase becomes an $\uparrow\downarrow$ -PN beyond a second critical field $h_{c2} > h_{c1}$. Our numerical results indicate that $h_{c1} \sim |\Delta_0|$ where $|\Delta_0|$ is evaluated at $h = 0$ for the same parameters.

In the strongly-interacting limit when $g \gg t$, it can be analytically shown for thermodynamic systems that $|\Delta_0| = (g/2 - 4t^2/g)\sqrt{n(2-n)}$, where $n = n_\uparrow + n_\downarrow$ is the total fermion filling. We checked that this thermodynamic expression agrees very well with our finite-lattice results, as it gives $|\Delta_0| \approx 7.23t$ for $\mu = 0$ or $n = 1$ and $|\Delta_0| \approx 7.18t$ for $\mu = -t$ or $n \approx 0.875$ when $g = 15t$, while we find, respectively, $|\Delta_0| \approx 7.25t$ and $|\Delta_0| \approx 7.19t$ for the same parameters in our BdG calculations. In the weakly-interacting limit when g is sufficiently small so that $\Delta_i \rightarrow 0$ for every i , we note that the system will be a \downarrow -vac for $h > 4t$ when $\mu = 0$ and for $h > 3t$ when $\mu = -t$. Next, we are ready to discuss the effects of balanced gauge fields.

B. Balanced Gauge Fields: $\phi_\uparrow = \phi_\downarrow \neq 0$

In Fig. 4, we present the $\phi_\sigma = 1/4$ phase diagrams for $\mu = 0$ in 4(a) and $\mu = -t$ in 4(b). The $\mu = 0$ case is very special since it corresponds to a half-filled lattice with particle-

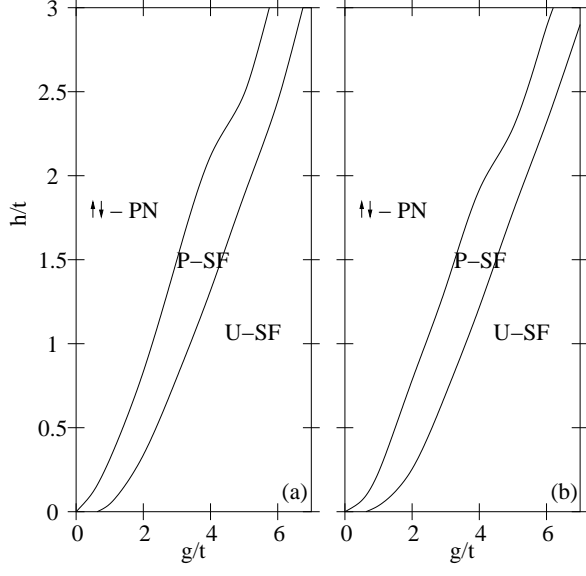


FIG. 3. (Color online) No gauge field: $\phi_\uparrow = \phi_\downarrow = 0$ case. The ground-state phase diagrams are shown for $\mu = 0$ in (a) and $\mu = -t$ in (b).

hole symmetry, where $n_{i\uparrow} + n_{i\downarrow} = 1$ independently of i , no matter what the rest of the parameters are. In comparison to Fig. 3, the $\phi_\sigma = 1/4$ diagrams have much richer structure involving large regions of stripe-ordered phases. To understand the physical origin of the resultant phase diagrams and stripe order, next we discuss the analytically tractable high- and low- h/g limits.

When h/g is sufficiently high, we can directly read off the single-particle ground state of the σ component from HB for any given ϕ_σ . For $\phi_\sigma = 1/4$, the energy spectrum consists of 4 bands: the σ component is a σ -vac for $\mu_\sigma \lesssim -2.83t$, a σ -N for $-2.83t \lesssim \mu_\sigma \lesssim -2.61t$, a σ -I(1/4) for $-2.61t \lesssim \mu_\sigma \lesssim -1.082t$, a σ -N for $-1.082t \lesssim \mu_\sigma \lesssim 1.082t$, a σ -I(3/4) for $1.082t \lesssim \mu_\sigma \lesssim 2.61t$, a σ -N for $2.61t \lesssim \mu_\sigma \lesssim 2.83t$ and a σ -I(1/1) for $2.83t \lesssim \mu_\sigma$. Using $\mu_\uparrow = \mu + h$ and $\mu_\downarrow = \mu - h$ in these expressions, the high- h/g structure of Fig. 4 immediately follows. As h/g gets smaller, the single-particle I and N phases must pave the way to ordered many-body ones, as increasing the strength of the pairing (attractive potential) energy eventually makes them energetically less favourable. For $\phi_\sigma = 0$, it is intuitively expected and numerically confirmed above that the $\uparrow\downarrow$ -PN to P-SF phase transition boundary $g(h_c)$ is a monotonic function of h , which is simply because the non-interacting system has a very simple band structure with cosine dispersions. However, due to the presence of multiple bands, the transition boundary $g(h_c)$ becomes a complicated function of h for finite ϕ_σ . For instance, we find a sizeable hump in Fig. 4(a) around $h \approx 2.7t$ and another one in Fig. 4(b) around $h \approx 1.7t$, the peak locations of which coincide intuitively with the $\uparrow\downarrow$ -PN regions that are sandwiched between VAC and/or I.

On the other hand, when h/g is sufficiently small, the ground state is expected to be an ordered many-body phase with no polarisation. In sharp contrast to the $\phi_\sigma = 0$ case

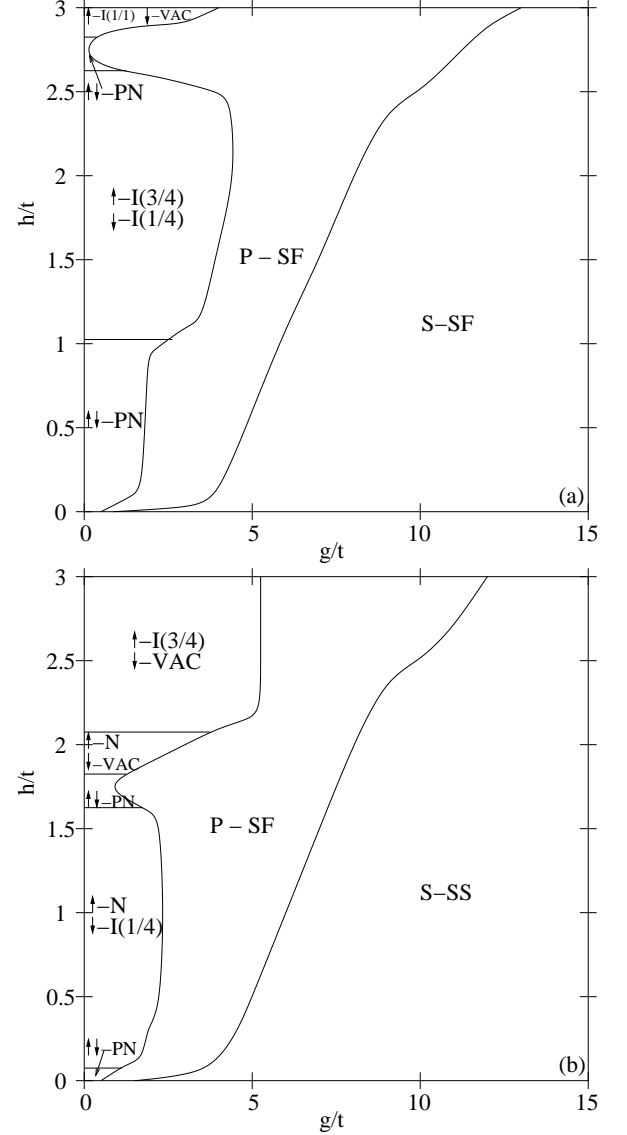


FIG. 4. (Color online) $\phi_\uparrow = \phi_\downarrow = 1/4$ case. The ground-state phase diagrams are shown for $\mu = 0$ in (a) and $\mu = -t$ in (b).

where U-SF is numerically confirmed above to be the ground state for any μ , we show in Fig. 4 that S-SF and S-SS are, respectively, stable for $\mu = 0$ and $\mu = -t$ when $\phi_\sigma = 1/4$. Note that since $\mu = 0$ corresponds to half filling for any ϕ_σ , the unpolarized ground states necessarily have uniform fillings, i.e., $n_{i\uparrow} = n_{i\downarrow} = 1/2$ for every i . Therefore, in the low- h/g limit, while only $|\Delta_i|$ is allowed to have spatial modulations in Fig. 4(a), both $|\Delta_i|$ and $n_{i\sigma}$ modulates in Fig. 4(b).

In comparison, the $\phi_\sigma = 1/6$ phase diagrams are shown in Fig. 5, and they are in many ways similar to the $\phi_\sigma = 1/4$ ones. The main difference is in the high- h/g limit which again directly follows from HB. For $\phi_\sigma = 1/6$, the energy spectrum consists of 6 bands: the σ component is a σ -vac for $\mu_\sigma \lesssim -3.076t$, a σ -N for a narrow band around $\mu_\sigma \approx -3.076t$, a σ -I(1/6) for $-3.076t \lesssim \mu_\sigma \lesssim -1.59t$, a σ -N for $-1.59t \lesssim \mu_\sigma \lesssim -1.41t$, a σ -I(1/3) for $-1.41t \lesssim \mu_\sigma \lesssim -0.65t$, a σ -N

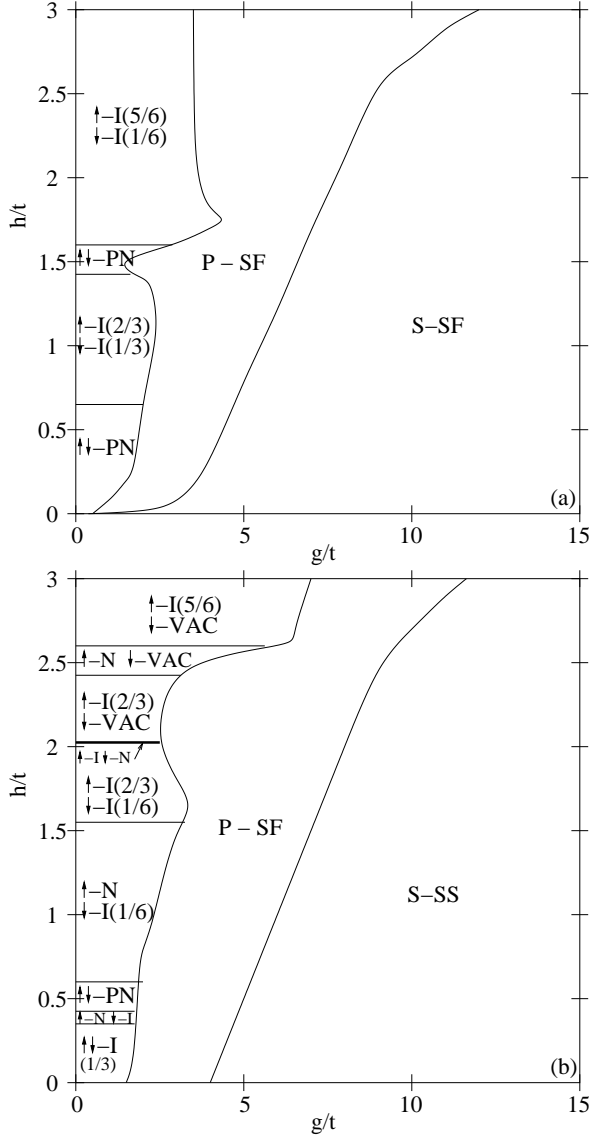


FIG. 5. (Color online) $\phi_\uparrow = \phi_\downarrow = 1/6$ case. The ground-state phase diagrams are shown for $\mu = 0$ in (a) and $\mu = -t$ in (b). Note in (b) the presence of a sliver of $\downarrow-N$ region around $h \approx 2.076t$.

for $-0.65t \lesssim \mu_\sigma \lesssim 0.65t$, a $\sigma-I(2/3)$ for $0.65t \lesssim \mu_\sigma \lesssim 1.41t$, a $\sigma-N$ for $1.41t \lesssim \mu_\sigma \lesssim 1.59t$, a $\sigma-I(5/6)$ for $1.59t \lesssim \mu_\sigma \lesssim 3.076t$, a $\sigma-N$ for a narrow band around $\mu_\sigma \approx 3.076t$ and $\sigma-I(1/1)$ for $3.076t \lesssim \mu_\sigma$. As a consequence of this, we note in Fig. 5(b) that the system intuitively requires a finite threshold for g/t even at $h = 0$, in order to develop any kind of many-body order. In addition, it is intriguing to see that the sliver of $\downarrow-N$ region that is sandwiched between $\downarrow-vac$ and $\downarrow-I(1/6)$ around $h \approx 2.076t$ gives rise to a sizeable hump in Fig. 5(b). This is clearly a result of increased single-particle density of states.

Note in Figs. 3-5 that the transition from an unpolarized to a polarized ordered phase occurs at a lower h for any given g as ϕ_σ is increased from 0. This is a consequence of smaller non-interacting energy bandwidths: as ϕ_σ increases from 0 to

$1/6$ to $1/4$ then W shrinks from $8t$ to $6.15t$ to $5.65t$, making it possible to polarize the ground state with a smaller and smaller h . In Figs. 4 and 5, the P-SF regions are dominated mainly by a phase that can be characterized by almost-stripped PDW and SDW orders with some additional corrugations along the stripes that is caused by $h \neq 0$. For instance, when this phase is nearby to an insulating one, it generally has a very small SDW order in the background on top of a large and uniform polarisation.

C. Imbalanced Gauge Fields: $\phi_\uparrow \neq \phi_\downarrow$

As we argued in Secs. I and II A, while independent control of the gauge fields ϕ_\uparrow and ϕ_\downarrow is not possible for conventional solid-state materials with real magnetic fields, such a control is plausible with neutral atomic systems. Motivated by this exotic possibility, here we study two different limits.

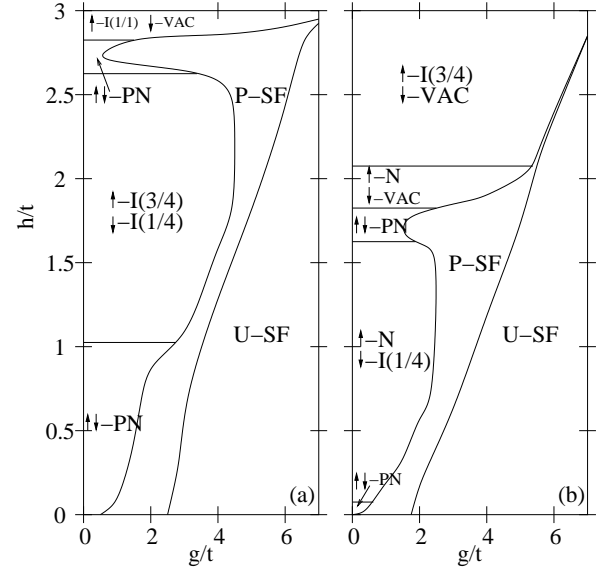


FIG. 6. (Color online) Time-reversal symmetric gauge fields: $\phi_\uparrow = -\phi_\downarrow = 1/4$ case. The ground-state phase diagrams are shown for $\mu = 0$ in (a) and $\mu = -t$ in (b).

As the first limit, we consider a pair of time-reversal symmetric gauge fields, i.e., $\phi_\uparrow = -\phi_\downarrow$. For instance, $\phi_\uparrow = 1/4$ phase diagrams are shown in Fig. 6, where we set $\mu = 0$ in 6(a) and $\mu = -t$ in 6(b). Thanks to the time-reversal symmetry, even though the ground state is not a P-SF but an unpolarized SF at $h = 0$, it is not properly indicated in these figures for low g/t . The general structures of the transition boundaries that are seen in these phase diagrams are quite similar to the ones shown in Fig. 4 for the $\phi_\uparrow = \phi_\downarrow = 1/4$ case. However, there is an important caveat in the dimer-BEC limit: the ground state becomes a U-SF for any μ as long as h/g is sufficiently low. Given our analysis in Sec. III B, this is intuitively expected since the effective gauge field of Cooper pairs vanish ($\phi_d = 0$) in the dimer-BEC limit as the gauge field of \uparrow and \downarrow fermions precisely cancel each other. In addition, the P-SF

regions necessarily shrink here, since the U-SF to P-SF transition boundaries are expected to be close to the no-gauge-field ($\phi_\sigma = 0$) ones shown in Fig. 3.

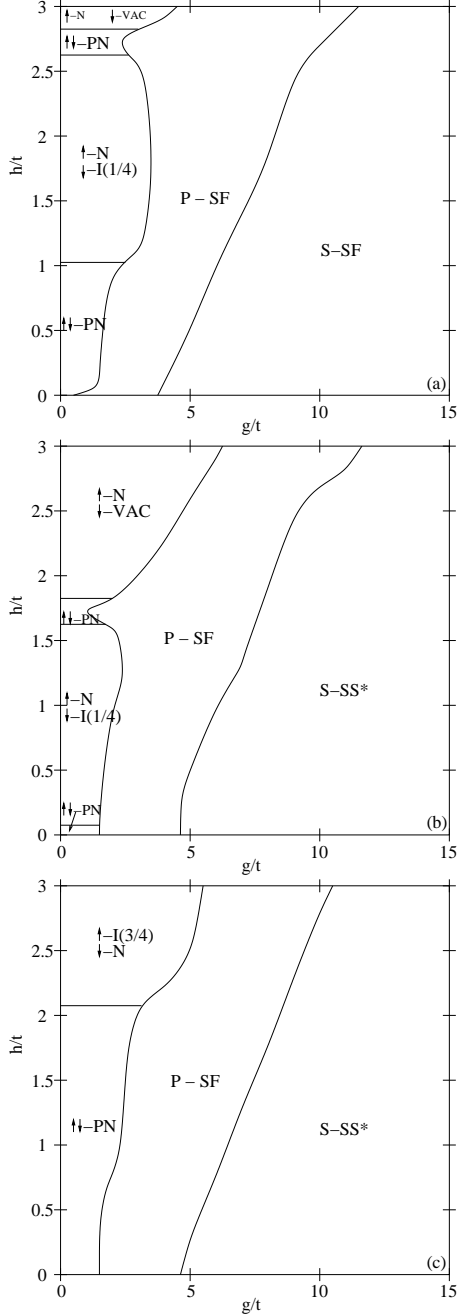


FIG. 7. (Color online) Charged-uncharged mixtures of fermions: $\phi_\uparrow = 0$ and $\phi_\downarrow = 1/4$ case in (a-b) and $\phi_\uparrow = 1/4$ and $\phi_\downarrow = 0$ case in (c). The ground-state phase diagrams are shown for $\mu = 0$ in (a) and $\mu = -t$ in (b-c). Thanks to the particle-hole symmetry, the $\phi_\uparrow = 1/4$ and $\phi_\downarrow = 0$ phase diagram for $\mu = 0$ can easily be deduced from (a) via $\uparrow \rightarrow \downarrow$ and $\downarrow \rightarrow \uparrow$.

As the second limit, we set one of the gauge fields to zero, corresponding effectively to a charged-uncharged mixture of two-component fermions. For instance, ($\phi_\uparrow = 0, \phi_\downarrow = 1/4$) phase diagrams are shown in Fig. 7, where we set $\mu = 0$ in

7(a) and $\mu = -t$ in 7(b), and ($\phi_\uparrow = 1/4, \phi_\downarrow = 0$) diagram is shown in Fig. 7(c) where we set $\mu = -t$. Thanks to the particle-hole symmetry around half-filling, ($\phi_\uparrow = 1/4, \phi_\downarrow = 0$) phase diagram for $\mu = 0$ can easily be deduced from 7(a) via $\uparrow \rightarrow \downarrow$ and $\downarrow \rightarrow \uparrow$, and therefore, it is not shown. Since this symmetry also prevents polarisation at $h = 0$, even though the ground state is not a P-SF but an unpolarized non-uniform (but non-stripped) SF for weak g/t , this is not properly indicated in Fig. 7(a). However, the imbalance between gauge fields causes P-SF in Figs. 7(b) and 7(c) even at $h = 0$. Similar to the analysis given in Sec. IV B, the high- and low- h/g limits can be directly read off from HB and effective dimer-BEC descriptions, respectively, with again an important caveat in the dimer-BEC limit: the ground state becomes a S-SS* for $\mu \neq 0$ as long as h/g is sufficiently low. As shown in Fig. 2(c), in addition to the coexisting striped-PDW and -CDW orders, S-SS* has an additional sign-changing striped-SDW order driven solely by $\phi_\uparrow \neq \phi_\downarrow$. Note also that if ($\phi_\uparrow \neq 0, \phi_\downarrow = 0$) then all of the coexisting orders of S-SS* phase are periodic along the y direction with periodicity $q_d = q_\uparrow$ since $\phi_d = \phi_\uparrow$.

D. Stripe Order vs. FFLO Modulations

It is clearly the cooperation between g , ϕ_\uparrow and ϕ_\downarrow that is responsible for the broken spatial symmetry and appearance of stripe order, causing much more prominent stripes for intermediate g at a given h . The stripe order is a direct result of HB: for a given ϕ_σ , the spectrum consists of q_σ -bands in the 1st magnetic Brillouin zone within which each \mathbf{k} state is q_σ -fold degenerate. Therefore, when $g \neq 0$, not only intra- and inter-band pairings but also pairings with both 0 and a set of non-zero center-of-mass momenta are allowed [21, 22], leading to a non-uniform $|\Delta_i|$ with spatially-periodic modulations, e.g, a PDW order [27]. The directions of center-of-mass momenta determine the direction of modulations, making it gauge dependent, e.g, y direction in Fig. 2. When the striped-PDW order is sufficiently large, it drives an additional striped-CDW order in the total fermion filling, giving rise to striped-SS phases.

We emphasise that the instabilities towards stripe-ordered phases discussed in this paper are driven by the gauge fields, and they may formally not be identified with the FFLO phase which is driven by the Zeeman field and is characterized by cosine-like sign-changing $|\Delta_i|$ oscillations along a spontaneously-chosen direction [28–30]. In addition, while the periods of our striped-PDW, -CDW and -SDW orders are always given by q_d , the period of FFLO modulations is determined by the mismatch h between \uparrow and \downarrow Fermi surfaces. For instance, when $\phi_\uparrow = \phi_\downarrow = p/q$, the stripes have a spatial period of q or $q/2$ lattice sites, depending on whether q is odd or even. Lastly, while our striped phases survive even in the extreme dimer-BEC limit ($g/t \gg 1$) for a large parameter space, the FFLO modulations survive not only in the BCS limit but also for a tiny parameter space nearby the P-SF to N transition boundary.

V. CONFINED ATOMIC SYSTEMS

Having explored the ground states and phase diagrams of thermodynamic systems, here we study confined systems and comment on the likelihood of observing stripe-ordered phases by loading neutral atomic Fermi gases on laser-induced optical lattices under laser-generated artificial gauge fields. For this purpose, we consider a harmonically-confined $51\ell \times 51\ell$ square lattice with an isotropic trapping potential $V_i = \alpha|\mathbf{r}_i|^2$ centered at the origin, where $\alpha = 0.01t/\ell^2$ is its strength and $\mathbf{r}_i \equiv (i_x, i_y)$ is the position of site i .

A. Effects of Harmonic Confinement

The local ground states of trapped systems can be reliably inferred through the so-called local-density approximation, where the local density of the system is mapped to that of a thermodynamic one with the same density. This description is known to be very accurate for large systems that are trapped in slowly-varying potentials. For our model Hamiltonian, due to the energy gaps of HB and the Pauli exclusion principle, one expects the so-called wedding-cake structures in $n_{i\uparrow}$ and $n_{i\downarrow}$ profiles of non-interacting fermions at $T = 0$, where the number of mini-gaps determines the number of spatially-flat $n_{i\sigma}$ regions for a given ϕ_σ . Thus, wedding-cake structures consist of a number of insulating regions that are sandwiched between normal regions. However, since the majority of these mini-gaps are very small compared to t , finite g and/or finite T quickly smear out the flat regions, making their detection nearly impossible. In sharp contrast, here we show that the broken spatial symmetry and stripe orders persist at intermediate and strong interactions, providing a viable knob for the experimental probe of the fractal structure of HB.

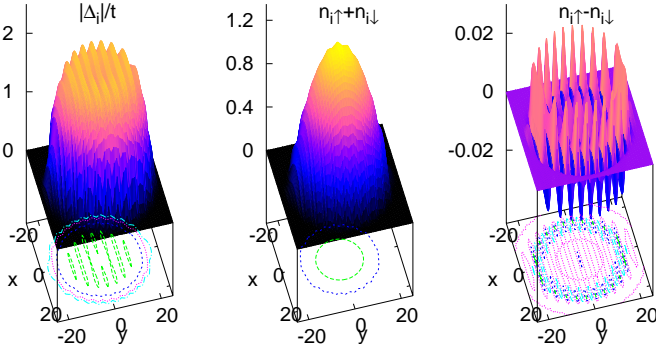


FIG. 8. (Color online) The trap profiles are shown for $\phi_\uparrow = 1/4$, $\phi_\downarrow = 0$, $\mu = t$, $h = 0$ and $g = 5t$. Here, (x, y) are in units of ℓ .

In Fig. 8, we illustrate a typical self-consistent solution for a trapped system when $\phi_\uparrow = 1/4$, $\phi_\downarrow = 0$, $\mu = t$, $h = 0$

and $g = 5t$. The total numbers of σ fermions are approximately given by $N_\uparrow = N_\downarrow \approx 464$. While the remnants of the so-called wedding-cake structure, i.e., spatially-flat $n_{i\uparrow}$ regions around integer multiples of $1/4$ fillings, are hardly recognisable, a large PDW order is clearly visible. Given the phase diagrams discussed in Sec. IV C, both CDW and SDW orders are expected to be weak around half-filling, since $n_{i\uparrow} + n_{i\downarrow} \gtrsim 1$ near the center of the trap for this particular set of data.

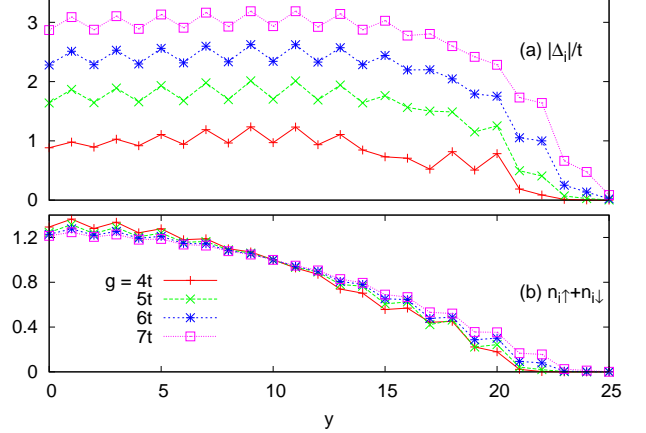


FIG. 9. (Color online) The trap profiles are shown for $x = 0$ cuts along the y direction which is in units of ℓ . Here, $\phi_\uparrow = \phi_\downarrow = 1/4$, $\mu = t$ and $h = 0$, and therefore, the system is locally unpolarized at every i .

It is easier to visualise and present such trap profiles for a cut along the y direction at a particular x value. For instance, we show $x = 0$ cuts in Figs. 9 and 10, where $\phi_\uparrow = 1/4$, $\mu = t$ and $h = 0$ in both figures, but $\phi_\downarrow = 1/4$ and $\phi_\downarrow = 0$, respectively. While the local ground states are always unpolarized in Fig. 9 where $n_{i\uparrow} = n_{i\downarrow}$ for every i , the imbalance between ϕ_\uparrow and ϕ_\downarrow causes small but visible SDW orders in Fig. 10. We note that $\phi_\uparrow \neq \phi_\downarrow$ may also cause a global polarisation, i.e., $N_\uparrow \neq N_\downarrow$, for weak g , however, this polarisation must gradually disappear towards the dimer-BEC limit. For instance, as g/t increases to (4, 5, 6, 7), while $N_\uparrow = N_\downarrow$ is approximately given by (454, 468, 491, 519) in Fig. 9, N_\uparrow and N_\downarrow are given, respectively, by (456, 464, 489, 518) and (448, 464, 489, 518) in Fig. 10.

These figures show that the CDW and SDW orders tend to be more prominent for intermediate g as long as the system is away from half-filling. This is quite intuitive since the appearance of a PDW order breaks the spatial symmetry of the system at the first place. The spatial periods are, respectively, given by 2 and 4 sites in Figs. 9 and 10, and these findings are in agreement with our analysis given in Sec. III B. In addition, since the relative stripes eventually fade away towards the dimer-BEC limit, the trap profiles slowly recover the usual (no-gauge-field) results in both figures. It is also pleasing to see that the valleys of the PDW and CDW orders and peaks of the SDW order coincide when they coexist. These results suggest that observation of PDW, CDW and SDW features as

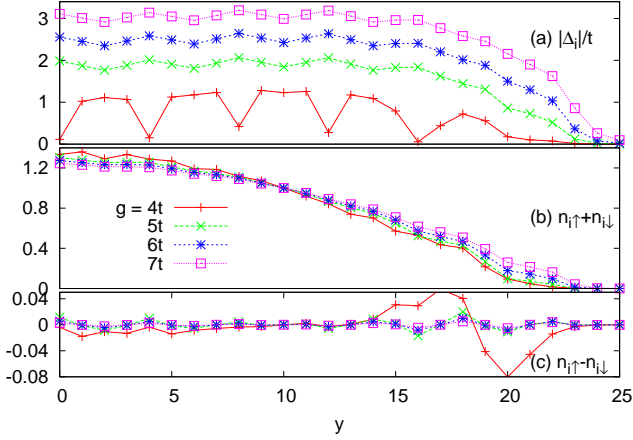


FIG. 10. (Color online) The trap profiles are shown for $x = 0$ cuts along the y direction which is in units of ℓ . Here, $\phi_\uparrow = 1/4$, $\phi_\downarrow = 0$, $\mu = t$ and $h = 0$.

a function of magnetic flux may furnish clearest and direct evidence for the existence of multiple band structure, and hence indirectly for the fractal HB, in trapped atomic systems.

B. Effects of Hartree Shifts

Since most of our phases have either coexisting CDW and/or SDW orders, our phase diagrams may not be convenient to generate more accurate phase diagrams by including the Hartree terms via a simple shift in $\mu_{i\sigma}$. However, we still neglected these shifts in our diagrams for their numerical as well as analytical simplicity. For instance, including these shifts in the self-consistency Eqs. (6)-(9) not only requires about an order of magnitude more iterations to converge, but also it complicates our current intuition making it more difficult to extract the relation between HB and the non-monotonic dependences of some of the phase boundaries. Note that since Hartree shifts have no role in driving the stripe-ordered phases, which is particularly clear in the dimer-BEC limit where $\mu_{i\sigma}$ do not explicitly play any role in our analysis, their inclusion is expected to change some of the transition boundaries without much effect on the stability of phases. Furthermore, since the mean-field theory provides only a qualitative description of the phase diagrams and the accuracy of our results can be somewhat improved by including these shifts, one still needs to go beyond this approximation for experimentally more relevant diagrams. Therefore, even though Hartree shifts are neglected in Sec. IV, our results may already pave the way to qualitative understanding of the exact ground states of the attractive Hofstadter-Hubbard model.

To illustrate these points, the Hartree-shifted trap profiles are shown in Figs. 11 and 12 for the parameters of Figs. 9 and 10, respectively. Comparing these figures show that while the inclusion of the Hartree shifts does not have much effect on $|\Delta_i|$ for these particular sets of data (thanks to the particle-hole symmetry around half-filling), it affects

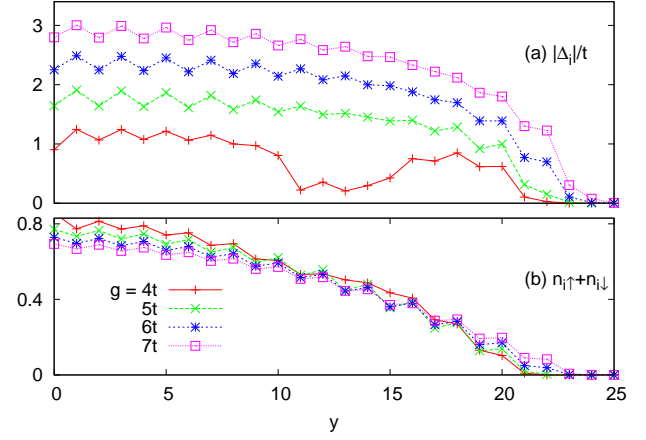


FIG. 11. (Color online) The trap profiles are shown for $x = 0$ cuts along the y direction which is in units of ℓ . Here, $\phi_\uparrow = \phi_\downarrow = 1/4$, $\mu = t$ and $h = 0$, i.e., same as Fig. 9 with the Hartree shifts included.

the total filling quite a bit. For instance, as g/t increases to (4, 5, 6, 7), while $N_\uparrow = N_\downarrow$ is approximately given by (288, 279, 279, 286) in Fig. 11, N_\uparrow and N_\downarrow are given, respectively, by (298, 278, 278, 285) and (276, 282, 278, 285) in Fig. 12. However, the visibility of the striped-PDW and -CDW orders remain largely the same in both cases. In addition, we note that the remnants of the wedding-cake structures, i.e., spatially-flat $n_{i\uparrow} + n_{i\downarrow}$ regions around $1/2$ fillings, are almost recognisable in Figs. 11(a) and 12(a) when $g = 4t$ or less (not shown). While the non-interacting \uparrow fermions are insulating at $1/4$ filling in both figures, the non-interacting \downarrow fermions are insulating (normal) in Fig. 11 (12). Thus, these insulating regions leave their traces as distinct $|\Delta_i|$ dips in both figures near $y = 13\ell$ when g is sufficiently weak.

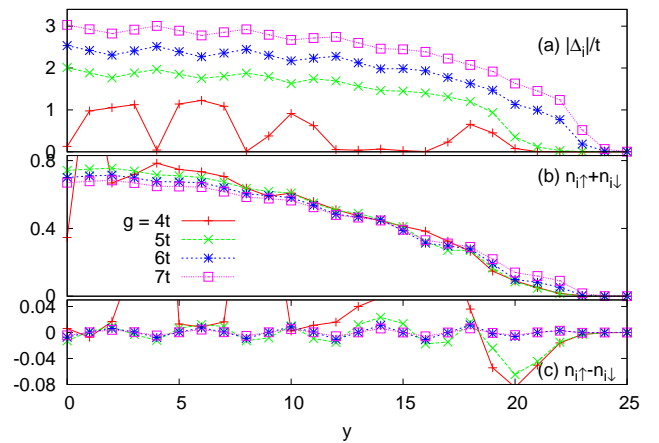


FIG. 12. (Color online) The trap profiles are shown for $x = 0$ cuts along the y direction which is in units of ℓ . Here, $\phi_\uparrow = 1/4$, $\phi_\downarrow = 0$, $\mu = t$ and $h = 0$, i.e., same as Fig. 10 with the Hartree shifts included.

Given these numerical illustrations, it is clear that our phase

diagrams already shed some light on a new stripe mechanism in the dimer-BEC limit, showing that the fate of stripe-ordered SF and SS phases are not affected by the Hartree terms. Having discussed the effects of confinement potentials, we are ready to end the paper with a briery summary of our conclusions and an outlook.

VI. CONCLUSIONS

Our mean-field results for the attractive single-band Hofstadter-Hubbard model on a square lattice are as follows. In the presence of a Zeeman field h , in addition to the intriguing phase transition boundaries between the N/I/VAC and SF phase, we found a number of distinct many-body phases which can be characterized with respect to their coexisting striped-PDW, -CDW and -SDW orders. Even at $h = 0$, we reached four important conclusions. First, we numerically found an unpolarized striped-superfluid phase (S-SF) in a large parameter space. Unlike the conventional FFLO phase which is driven by h , our S-SF is driven only by the gauge fields. Second, we numerically found an unpolarized striped-supersolid phase (S-SS) in a large parameter space. Unlike the conventional SS phase which is yet to be observed and is driven either by long-range (e.g., nearest-neighbor) interactions or the presence of a second species (e.g., Bose-Fermi or Bose-Bose mixtures), our S-SS is again driven only by the gauge fields. Third, we also found a locally polarized but globally unpolarized striped-SS phase (S-SS*) when the gauge fields are imbalanced. Lastly, we provided analytical insights on the microscopic origins of these stripe-ordered phases, suggesting a new physical mechanism that gives rise to FFLO-like SF and SS phases in the dimer BEC limit.

The importance of these results can be highlighted as follows. First, spatially-modulated SF and SS phases are both of high interest not only to the atomic physics community but also to the condensed-matter, nuclear and elementary-particle physics communities. Second, the unusual appearance of the stripe order is very exotic and fundamentally important by itself, because the connection between the striped-charge order that is observed in copper-oxide materials and the formation of high- T_c superconductivity has been the subject of a long debate in the literature. Even though our work offers no direct relation to cuprate superconductors, understanding stripe-ordered phases in the cold-atom context may still prove to be beneficial for the high- T_c community. Third, the existence of stripe-ordered phases is not an artefact of our mean-field BdG description, since they are analytically motivated in the dimer-BEC limit. Therefore, we highly encourage further research in this direction with different lattice geometries, gauge fields, etc., in particular the beyond mean-field ones.

ACKNOWLEDGMENTS

This work is supported by TÜBİTAK Grant No. 1001-114F232, and the author thanks Dr. R. O. Umucalılar for discussions.

Appendix A: Dimer-BEC Limit in the Symmetric Gauge

It may be important to remark here that the analysis given in Sec. IIIB depends on the particular artificial gauge field that is simulated in a cold-atom experiment. Next, we use a rotationally-invariant symmetric gauge for the vector potential, i.e. $\mathbf{A}_\sigma(\mathbf{r}) \equiv B_\sigma(-y, x, 0)/2$, and analyse the spatial structure of the order parameter $|\Delta_i|$ in the dimer-BEC limit, which clearly reveals this dependence.

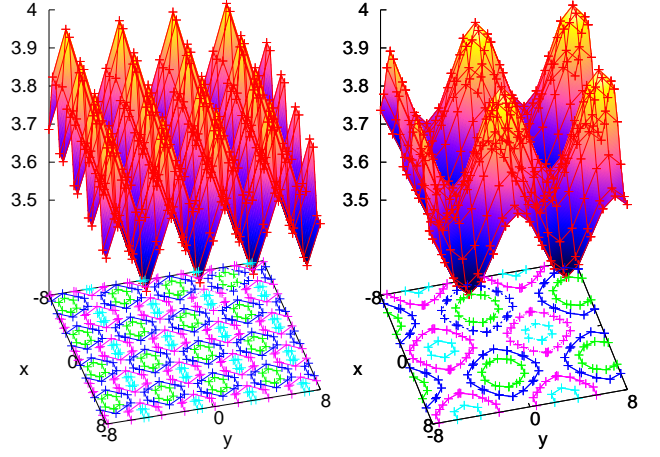


FIG. 13. (Color online) Typical $|\Delta_i|/t$ profiles are shown for the checkerboard-like stripes, where $\phi_\uparrow = \phi_\downarrow = 1/4$ in the left and $1/8$ in the right figure as determined by the symmetric gauge. Here, (x, y) are in units of ℓ , and we set $\mu = 0$, $h = 0$ and $g = 8t$ in both figures.

Typical $|\Delta_i|$ profiles are illustrated in Fig. 13 for $\phi_\sigma = 1/4$ and $1/8$, i.e. $\phi_d = \phi_\uparrow + \phi_\downarrow \equiv p_d/q_d$ is $1/2$ and $1/4$, respectively. Since the C_4 symmetry of the square lattice is preserved in this gauge, the stripes are checkerboard-like in the (x, y) plane, such that generalisation of Eq. (10) to

$$|\Delta_i| = |\Delta_0| + |\Delta_1| [2 - \cos(\pi\phi_d i_x/\ell) - \cos(\pi\phi_d i_y/\ell)] \quad (\text{A1})$$

fits very well with all of our numerical results in the dimer-BEC limit. Here, the uniform contribution $|\Delta_0| = (g/2 - 4t^2/g)\sqrt{n(2-n)}$ is determined by the total average filling n with $\mu = (g/2 - 8t^2/g)(n-1)$ [26], $|\Delta_1| \approx t^2/g$ for $\mu \approx 0$, and $\mathbf{r}_i \equiv (i_x, i_y)$ is the position of site i . We again note that this analytical expression is consistent with our expectation that while the dimer-BEC order parameter in principle has contributions from all degenerate momenta $\Psi_{id} = \sum_{\mathbf{k}_d} c_{\mathbf{k}_d} e^{i\mathbf{k}_d \cdot \mathbf{r}_i}$, where $c_{\mathbf{k}_d} = |c_{\mathbf{k}_d}| e^{i\vartheta_{\mathbf{k}_d}}$ are complex variational parameters, only the lowest order $\mathbf{k}_d = \{(0, 0); \pi\phi_d(f_x, f_y)/\ell\}$ terms contribute when g/t is sufficiently large. This is because dimer bosons are fermion pairs and the number of ways of creating them with $\mathbf{k}_d = \mathbf{k}_\uparrow + \mathbf{k}_\downarrow$ momentum depends on f_x, f_y, ϕ_\uparrow and ϕ_\downarrow , and higher \mathbf{k}_d states contribute less and less, forming again a perturbative series.

In addition, moving towards the BCS side, the second-order corrections to Eq. (A1) can be shown

to be $+|\Delta_2|[\cos(2\pi\phi_d i_x/\ell) + \cos(2\pi\phi_d i_y/\ell)]$ and $+|\Delta'_2|\cos(\pi\phi_d i_x/\ell)\cos(\pi\phi_d i_y/\ell)$ for any q_d . Since these terms are in- (out-of- π -) phase with the zeroth (first) order term, they tend to create dimples at the peaks arising from the first order one, suggesting that $\vartheta_{\mathbf{k}_d} - \vartheta_0 = \pi(f_x + f_y)$,

i.e., the form of $|\Psi_{id}|$ again coincides with $|\Delta_i|$ under these conditions. Finally, we note that both our numerical results as well as the analytical fit Eq. (A1) clearly show that modulations of $|\Delta_i|$ have a spatial period of $2q_d$ lattice sites along both x and y directions, as expected for the resultant dimers in the symmetric gauge.

-
- [1] D. R. Hofstadter, Phys. Rev. B **14**, 2239 (1976).
 - [2] M. Kohmoto, Phys. Rev. B **39**, 11943 (1989).
 - [3] C. R. Dean *et al.*, Nature **497**, 598 (2013).
 - [4] L. A. Ponomarenko *et al.*, Nature **497**, 594 (2013).
 - [5] V. Galitski and I. B. Spielman, Nature **494**, 49 (2013).
 - [6] J. Dalibard, F. Gerbier, and G. Juzeliūnas, and P. Öhberg, Rev. Mod. Phys. **83**, 1523 (2011).
 - [7] J.-Y. Zhang, S.-C. Ji, Z. Chen, L. Zhang, Z.-D. Du, B. Yan, G.-S. Pan, B. Zhao, Y.-J. Deng, H. Zhai, S. Chen, and J.-W. Pan, Phys. Rev. Lett. **109**, 115301 (2012).
 - [8] P. Wang, Z.-Q. Yu, Z. Fu, J. Miao, L. Huang, S. Chai, H. Zhai, and J. Zhang, Phys. Rev. Lett. **109**, 095301 (2012).
 - [9] L. W. Cheuk, A. T. Sommer, Z. Hadzibabic, T. Yefsah, W. S. Bakr, and M. W. Zwierlein, Phys. Rev. Lett. **109**, 095302 (2012).
 - [10] C. Qu, C. Hamner, M. Gong, C. Zhang, and P. Engels, Phys. Rev. A **88**, 021604(R) (2013).
 - [11] Z. Fu, L. Huang, Z. Meng, P. Wang, X.-J. Liu, H. Pu, H. Hu, and J. Zhang, Phys. Rev. A **87**, 053619 (2013).
 - [12] R. A. Williams, M. C. Beeler, L. J. LeBlanc, K. Jiménez-García, and I. B. Spielman, Phys. Rev. Lett. **111**, 095301 (2013).
 - [13] K. Jiménez-García, L. J. LeBlanc, R. A. Williams, M. C. Beeler, A. R. Perry, and I. B. Spielman, Phys. Rev. Lett. **108**, 225303 (2012).
 - [14] J. Struck, C. Ölschläger, M. Weinberg, P. Hauke, J. Simonet, A. Eckardt, M. Lewenstein, K. Sengstock, and P. Windpassinger, Phys. Rev. Lett. **108**, 225304 (2012).
 - [15] C. J. Kennedy, G. A. Siviloglou, H. Miyake, W. C. Burton, and W. Ketterle, Phys. Rev. Lett. **111**, 225301 (2013).
 - [16] M. Aidelsburger, M. Atala, M. Lohse, J. T. Barreiro, B. Paredes, and I. Bloch, Phys. Rev. Lett. **111**, 185301 (2013).
 - [17] H. Miyake, G. A. Siviloglou, C. J. Kennedy, W. C. Burton, and W. Ketterle, Phys. Rev. Lett. **111**, 185302 (2013).
 - [18] C. Chin and E. J. Mueller, Physics **6**, 118 (2013).
 - [19] D. Cocks, P. P. Orth, S. Rachel, M. Buchhold, K. Le Hur, and W. Hofstetter, Phys. Rev. Lett. **109**, 205303 (2012).
 - [20] L. Wang, H.-H. Hung, and M. Troyer, Phys. Rev. B **90**, 20511 (2014).
 - [21] Hui Zhai, R. O. Umucalılar, and M. O. Oktel, Phys. Rev. Lett. **104**, 145301 (2010).
 - [22] R. Wei and E. J. Mueller, Phys. Rev. Lett. **108**, 245301 (2012).
 - [23] M. Iskin, Phys. Rev. A **91**, 011601(R) (2015); and also see arXiv:1406.6890v1 (2014).
 - [24] T. Esslinger, Annu. Rev. Condens. Matter Phys. **1**, 129 (2010).
 - [25] S. Powell, R. Barnett, R. Sensarma, and S. Das Sarma, Phys. Rev. Lett. **104**, 255303 (2010).
 - [26] M. Iskin and C. A. R. Sá de Melo, Phys. Rev. A **78**, 013607 (2008).
 - [27] D. F. Agterberg and H. Tsunetsugu, Nature Phys. **4**, 639 (2008).
 - [28] P. Fulde and R. Ferrell, Phys. Rev. **135**, A550 (1964).
 - [29] A. I. Larkin and Y. N. Ovchinnikov, Sov. Phys. JETP **20**, 762 (1965).
 - [30] R. Casalbuoni and G. Nardulli, Rev. Mod. Phys. **76**, 263 (2004).